The Formation, Evolution, and Sustainment of Inlet Ground Vortices

Derek A. Nichols[1], Bojan Vukasinovic[2], and Ari Glezer[3]
Georgia Institute of Technology, Atlanta, GA 30332-0405

Abstract

The formation and sustainment of a ground vortex in the cross flow normal to an axisymmetric nacelle near a ground plane is investigated in wind tunnel experiments. It is shown that the vortex formation is precipitated by the development of countercurrent shear flow that is induced over the ground plane on the leeward side of the nacelle by interactions between the streamwise cross flow and the nacelle suction, once the nacelle's near wake closes onto the ground plane. The countercurrent flow engenders wall-normal rollup of boundary layer vorticity concentrations that, depending on the direction of the prevailing countercurrent velocity, are advected either downstream or towards the nacelle where they become anchored and are ingested into its inlet. The anchored ground vortex is sustained by the transport, reorientation, and stretching of boundary layer vorticity that is funneled off the ground plane by the vortex-induced flow and becomes aligned with the vortex axis while, thereafter, preserving its circulation.

Nomenclature

D	=	inlet plane diameter
h	=	ground plane distance from inlet base
$\dot{m}$	=	inlet mass flow rate
$\dot{m}_c$	=	inlet mass flow rate at choking
$\dot{m}^*$	=	$\dot{m}/\dot{m}_c$
$\dot{P}$	=	inlet momentum flux
$\dot{P}^*$	=	dimensionless inlet momentum flux
$\dot{P}_o^*$	=	dimensionless inlet momentum flux required to form vortex
r	=	radial distance from inlet centerline
r'	=	radial distance from vortex center
R	=	inlet plane radius
R_v	=	ground vortex radius
t	=	time
$\bar{u}$	=	mean tunnel streamwise velocity component
U_o	=	crosswind speed
V	=	average inlet velocity
V_{mag}	=	velocity magnitude at shear layer interface
V_n	=	ground vortex centerline velocity
x	=	horizontal displacement from inlet centerline
y	=	streamwise displacement from inlet face
z	=	vertical displacement from inlet centerline
z'	=	vertical displacement from ground plane
Γ	=	ground vortex circulation
ζ	=	ground vortex centerline vorticity
θ	=	azimuthal coordinate
ρ	=	ambient air density
ω_y	=	spanwise vorticity
ω_z	=	cross-stream (wall normal) vorticity

[1] Graduate Research Assistant, AIAA Member.
[2] Senior Research Engineer, AIAA Member.
[3] Professor, AIAA Fellow.

I. Background

Engine nacelles of commercial aircraft must be designed to comply with the Code of Federal Regulations (CFRs) throughout all stages of flight including ground taxi, takeoff, climb, cruise, descent, and landing. Although most of the flight duration is spent in cruise, the critical design of the nacelle must accommodate operation at lower aircraft speeds during takeoff, landing, and ground operations when the performance of the engines can be strongly impacted by crosswind that can significantly alter the air intake at the inlet (Trapp et al., 2006). At low speed, the crosswind can lead to the formation of a fuselage vortex and induce inlet flow separation (even away from the ground) and near the surface can form a ground vortex (Colehour & Farquhar, 1971; Trapp & Girardi, 2012).

Once formed, the ground vortex induces distortion within the engine face and can also lead to the ingestion of foreign objects into the engine. As noted by Colehour and Farquhar (1971), about 50% of all engines removed from aircraft for maintenance or repair had been damaged by foreign object ingestion that was previously investigated by Klein (1953). Ground vortex formation with varying engine height above ground and engine and crosswind speeds was investigated by Rodert and Garret (1955) who suggested that the formation required a stagnation line off the ground plane. This stagnation line is formed when the inlet's capture surface reaches and subsequently interacts with the ground plane (Siervi, 1981). Johns (2002) discusses how the capture surface can change in the presence of a crosswind, headwind, or tailwind. The work of Liu et al. (1985) demonstrated a linear relationship between the ratio of the mean intake and crosswind speeds, V/U_∞, for which a ground vortex first forms and the ratio of the inlet elevation above ground to its diameter, H/D. Similar findings were reported by Shin et al. (1986) for inlets of varying size and orientation, and Nakayama and Jones (1996, 1999) improved this fit further and included data for small H/D and high Mach numbers.

The earlier investigations indicated that the flow characteristics of the ground vortex vary with the three formation parameters namely, the engine height above ground, the engine speed, and the crosswind speed. These parameters were investigated by Shin et al. (1986) who measured the ground vortex circulation in wind tunnel experiments while varying V/U_∞, and H/D and reported that the vortex strength, as measured by its circulation, increases with V/U_∞ and decreases with H/D. Brix et al. (2000) performed comprehensive wind tunnel experiments and noted that the circulation of the vortex increases by increased circulation around the inlet with U_∞ or by increased vortex stretching with the intake velocity V. Siervi et al. (1982) suggested that there are two competing mechanisms for the inlet vortex formation associated with the variation of circulation along the nacelle by the crosswind or with the ingestion of the ground boundary layer vorticity. In experiments to investigate the former, two inlets were placed on top of one another in the absence of a ground plane. The authors reported that a vortex formed between them and concluded that the surface boundary layer was not the primary source of vorticity that leads to vortex generation. In later numerical investigations, Trapp and Girardi (2012) verified that the formation of the vortex depends on the presence of a source of vorticity in the flow field and showed that this vorticity source can come from either the ground or the outer surface of the nacelle while noting that the vorticity generated on the nacelle's surface contributes more to the ground vortex circulation than vorticity that is transported off the ground.

Murphy et al. (2010) studied the effect of a horizontally moving ground plane to simulate realistic takeoff conditions at low velocity ratios between the crosswind and intake speeds and noted that, compared to a stationary ground plane, a ground vortex on a moving ground plane was weaker,

steadier, and more symmetric relative to the static ground. Murphy and MacManus (2011) considered the effects of the ground plane distance and the yaw angle of the crosswind and showed that a stronger vortex formed at lower ground plane clearances and higher intake yaw angles. Several numerical studies investigated suppression of the ground vortex using external air jets on the nacelle including fan reverser jets (Johns, 2002; Shmilovich & Yadlin, 2006) and pulsed jets (Johns, 2002; Shmilovich & Yadlin, 2011). Notably, the simulations of Shmilovich & Yadlin (2006, 2011) indicated that ground vortex ingestion could be prevented by using 'sprinkler' jet actuation.

The present experimental investigation is a continuation of the earlier works of Nichols et al. (2022, 2023) that focused on the formation, characterization, and scaling properties of ground vortices that are formed by the interaction of the nacelle and cross flow in close proximity to a ground plane. While the prior investigations focused on exploration of the parameter space for the appearance of ground vortices (Nichols et al., 2022) and a formation map in terms of the critical dimensionless parameters (Nichols et al., 2023), the present work explores further the underlying flow mechanisms that lead to formation and advection of ground vortices and to the sustainment of these vortices once they are anchored to the nacelle.

II. Experimental Setup and Flow Diagnostics

The present experimental investigation is conducted in an open-return wind tunnel that was designed for studies of the flow physics of nacelles in crosswind (Figure 1a). The cross flow in the test section is driven by an axial blower through a 10:1 ratio contraction [the flow uniformity in the empty test section is within 1% (Nichols et al., 2019)] The axisymmetric nacelle model has an inlet plane diameter D = 19.4 cm (with a centerbody of diameter 0.27D) and is mounted on an axisymmetric duct that is driven in suction by a blower where the exhaust air is released into the space through chilled water heat exchangers such that the ambient air temperature is maintained to within 1°C. The nacelle blower is driven at a prescribed mass flow rate $\dot{m}$ that is monitored using a pitot probe assembly within a calibrated straight pipe segment upstream of the blower's inlet. The entire nacelle blower assembly is mounted on a moveable cart that enables axial and lateral adjustments of the nacelle's protrusion within the wind tunnel's test section (cross section 106 x 106 cm and 305 cm long, Figure 1b). In the present investigation, the nacelle model is oriented normal to the cross flow and extends through half the width of the test section. The bottom surface of the wind tunnel's test section is formed by a motorized, vertically-adjustable (to within 0.25 mm) ground plane that can be lowered down to $h = 1.45D$ below the bottom edge of the nacelle (Figure 2a).

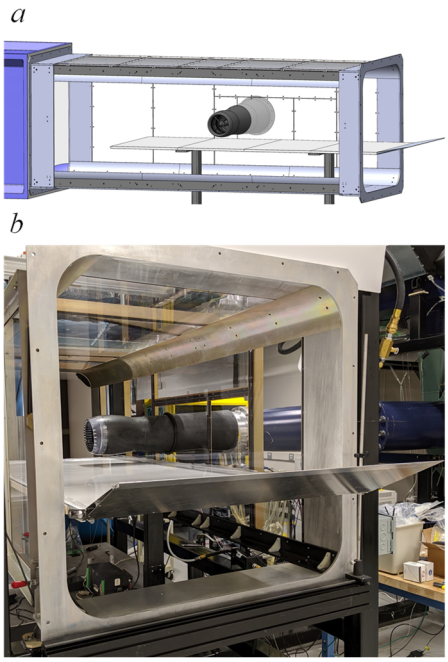

Figure 1. *Upstream view of the wind tunnel's test section showing the installed axisymmetric nacelle inlet model and the vertically-adjustable ground plane.*

In the present investigations the nacelle is operated up to $M = 0.33$ (the maximum nacelle Mach number is 0.7) and the flow within the nacelle is characterized by the mass flow ratio $\dot{m}^* = \dot{m}/\dot{m}_c$ ($\dot{m}_c$ = 12.4 lb/sec is measured at choking) which is varied between 0.16 and 0.65 while the tunnel's

cross flow speed U_o is varied between 10 and 30 kt. The motion of the ground vortex and its velocity field are extracted from planar and stereo particle image velocimetry (PIV) in planes that are parallel either to the ground plane or to the inlet's face as illustrated schematically in Figures 2b and c, respectively. The PIV cameras and laser optics are placed on computer-controlled traverses that enable data acquisition in multiple planes.

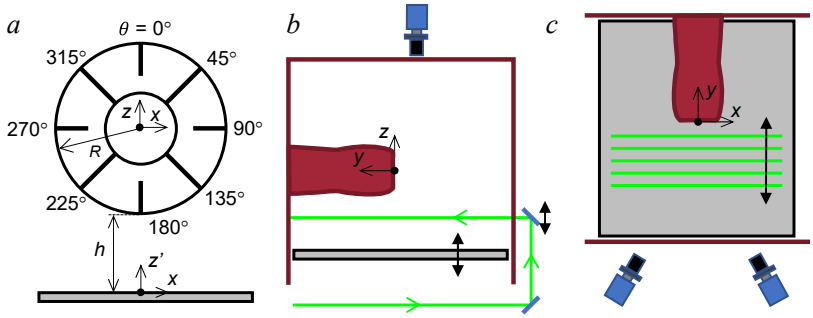

Figure 2. *a) Schematic front view of the nacelle's inlet above the ground plane showing the centerbody and the azimuthal angle θ; b) Schematic rendition of planar PIV in planes that are parallel to the ground plane showing the laser sheet and the CCD camera; and c) Stereo PIV setup using sheet illumination in planes that are parallel to the inlet face and the stereo CCD cameras.*

III. Formation of the Ground Vortex

As shown by earlier investigators, the complex interaction of an inlet in a crosswind in close proximity to the ground plane during takeoff, landing, and ground roll can lead to the formation of a ground vortex (e.g., Colehour & Farquhar, 1971). Figures 3a and b show images of vertical and horizontal cross sections of a ground vortex captured in the wind tunnel (corresponding to Figures 2c and b, respectively) when the crosswind flow in the test section (from left to right) is seeded with theatrical fog and illuminated by a laser sheet. Figure 3a shows the tilting and ingestion of the clockwise (CW) vortex into the nacelle above its lower lip. Owing to the inlet speed and the angular velocity, the concentration of the seed particles within the vortex core is evidently lower, but because of the lower pressure within the core, it is marked by a ring of condensed water vapor. An image of the cross section of the vortex in the horizonal plane $0.13D$ above the ground plane (Figure 3b) shows the advection of cross flow fluid into the vortex that is subsequently tilted along the core towards the nacelle's inlet (cf. Section IV).

The flow conditions that lead to the onset of ground vortices that are either advected downstream or form a nominally stationary vortex that is ingested into the nacelle were investigated by Nichols et al. (2022) who showed that the appearance of a vortex depends on three formation parameters namely, the inlet mass flow rate, crosswind speed, and distance between the nacelle and ground plane. The authors showed that these parameters can be combined into two dimensionless groups: the ratio of the inlet to cross stream momentum fluxes at which the vortex first forms, $\dot{P}_o^* = (\dot{m}V/\rho U_o^2 D^2)_o$, and the ratio of the inlet plane diameter to nacelle height above the ground

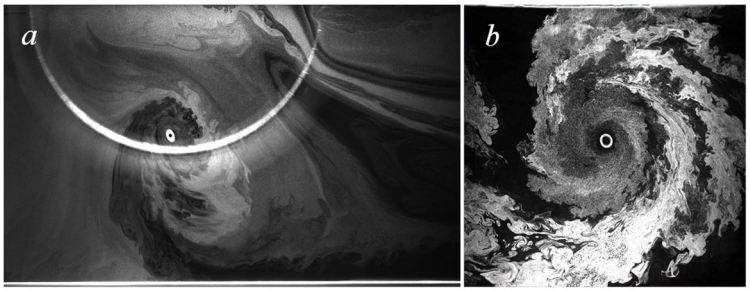

Figure 3. *Sectional images of the ground vortex visualized by particle seeding within a laser sheet: a) Vertical plane at the inlet face showing the ingested vortex, and b) Horizontal sample image of the fog-seeded ground vortex with cross flow moving from left to right.*

plane, D/h. Together, these two parameters can be used to mark the boundary beyond which ground vortices are formed within the flow as depicted in a formation map that is reproduced in Figure 4. As noted by Nichols et al. (2023), the use of the momentum flux ratio rather than the ratio of the inlet and crosswind speeds that implicitly excludes density variations (e.g., Nakayama & Jones, 1996, Liu et al., 1985 and Shin et al., 1986) may better convey the asymptotic behavior of this boundary. The data in Figure 4 show that, at any given nacelle D/h, there is a critical $\dot{P}_o^*$ above which a vortex is formed. The limit as (D/h) decreases indicates that the inlet momentum flux (or engine thrust) must increase sharply to form a ground vortex when the nacelle height above the ground plane increases, indicating that a ground vortex eventually becomes unattainable. As (D/h) increases or the nacelle distance decreases, the inlet momentum flux (or engine thrust) needed for vortex formation decreases and asymptotically approaches a small but finite thrust indicating that a ground vortex can form even at vanishingly small h and a very low engine thrust. The data in Figure 4 show that the boundary for the formation of ground vortices can be represented by $\dot{P}_o^* = 375(h/D)^2$.

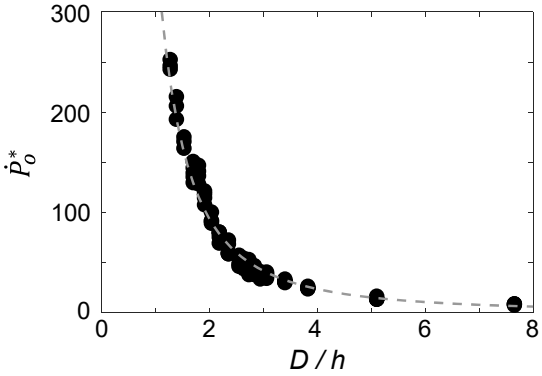

Figure 4. *Formation map showing the boundary beyond which (above and to the right) ground vortices are formed within the flow. A least squares fit to the data is shown using a dashed line.*

The earlier investigations of Nichols et al. (2022) showed that ground vortices can be engendered by a countercurrent shear layer that forms within the ground plane boundary layer as a result of interactions between the streamwise cross flow and the opposing flow induced by the suction into the nacelle. The dependence of the vortex formation on the presence of opposing time-averaged streamwise velocity $\bar{u}$ was investigated using planar PIV measurements in a horizontal plane $z' = 0.10D$ above the ground plane. As an indication of the countercurrent flow, the variation of the time-averaged streamwise velocity along x at $y = 0$ is measured for five values of the dimensionless momentum flux ($\dot{P}^* = 23$, 42, 61, 82, and 197) indicated in Figure 5a relative to the formation boundary. For this fixed ground plane distance of $h/D = 0.33$, the formation map indicates that ground vortices would only form for $\dot{P}^* > 40$. The variation of the streamwise velocity near the ground for each of these parameters is shown in Figure 5b. At $\dot{P}^* = 23$, ground vortices do not form as indicated by the absence of reversed $\bar{u}$ near the surface. When $\dot{P}^* = 42$, the momentum flux is just above the formation boundary ($\dot{P}_o^* = 40$) and ground vortices form occasionally but do not consistently establish a quasi-stable vortex that is ingested into the inlet, and the trace of

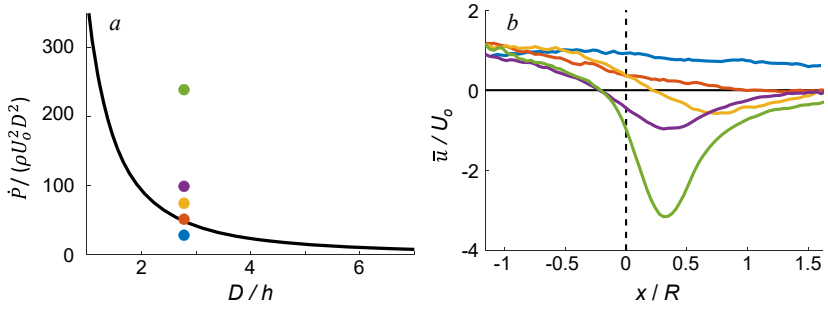

Figure 5. *a) Selected five formation parameters for ground vortices shown on the formation map; and b) The corresponding variation of the time-averaged streamwise velocity along x at $z'/D = 0.10$ and $y = 0$ for $\dot{P}^* = 23$ (●), 42 (●), 61 (●), 82 (●), and 197 (●) and $U_o = 10$ kt. The position of the inlet's vertical centerline is shown by the dashed line for reference.*

$\bar{u}$ in Figure 5b exhibits weak reversed streamwise flow above the surface at the downstream edge of the measurement domain ($x/R > 1$). As $\dot{P}^*$ is increased, the magnitude of the reversed flow near the surface intensifies substantially and is indicative of upstream advection of vortices and the anchoring of a nominally-stable ground vortex that is ingested into the inlet. It is also noteworthy that as $\dot{P}^*$ is increased further, the peak level of the $\bar{u}$ migrates upstream towards $x = 0$. As shown by Nichols et al. (2023), even further increase in $\dot{P}^*$ leads to the continuous upstream migration of the ingested ground vortex towards the windward side of the inlet and its eventual dislodging.

The presence of the countercurrent shear layer when $\dot{P}^* = 42$ ($h/D = 0.33$, $U_o = 30$ kt) is demonstrated in Figure 6a using a color raster plot of the time-averaged magnitude of the in-plane velocity in the plane $z'/D = 0.13$ (the field of view is centered around $x/R = 1.5$, $y/R = -0.8$ and measures $1.4R \times 1.4R$ as illustrated in the figure). As noted in connection with Figure 5, $\dot{P}^* = 42$ is just above $\dot{P}_o^*$ for this ground plane distance but below the $\dot{P}^*$ needed for the formation of a stable, ingested vortex. These data clearly show the reversed flow induced by the suction into the nacelle once the nacelle's near wake closes on the ground plane (Nichols et al., 2023), which is separated from the cross flow by a band of low levels of V_{mag} about the zero streamline ($V_{mag} = 0$, shown using a solid line). It is important to note that the countercurrent flow of the instantaneous velocity fields is migrating along the span of the flow such that the instantaneous zero streamline is meandering along the y-coordinate in Figure 6a. The time-averaged zero streamlines for three levels of $\dot{P}^*$ (42, 43, and 45) above the critical momentum flux ($\dot{P}_o^* = 40$) for this ground plane elevation but before the formation of a nominally-stable ground vortex are plotted in Figure 6b and exhibit increasing streamwise displacement relative to the inlet with increasing $\dot{P}^*$. The instantaneous velocity fields for the three levels of $\dot{P}^*$ are used for detection of instantaneous wall-normal vortices. The process involves using proper orthogonal decomposition (POD) as a low-pass filter to focus on the dominant flow features in reconstructed flow fields (Sirovich, 1987; Berkooz et al., 1993) that preserve 67% of the original flow energy in the ten highest order modes. For each of these instantaneous POD-reconstructed velocity fields, vortical structures are identified and tracked using the Γ_1 criterion (Graftieaux et al., 2001; Huang & Green, 2015) which identifies rotational motions in the velocity field. Locations of the vortex cores are computed from the weighted average of the Γ_1 data that exceeds a predetermined threshold. Sequential records of POD-reconstructed PIV data are then used to inform the locations where a vortex forms and allows for tracking of its motion in subsequent instances. The locations of initial vortex formation are overlaid for the multiple sequences of $\dot{P}^*$ in Figure 6b and show that they are clearly correlated with the corresponding zero velocity streamlines of the countercurrent flow, thereby substantiating the

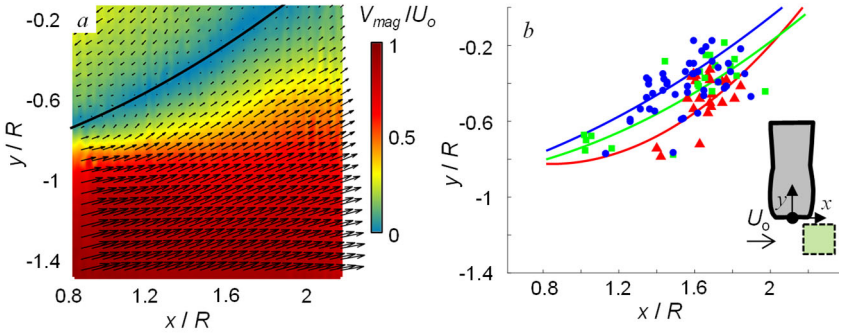

Figure 6. *a) Color raster plot of the time-averaged magnitudes of the two velocity components overlaid with the velocity vectors in the plane $z'/D = 0.13$ for $h/D = 0.33$ and $\dot{P}^* = 42$. The zero streamline is shown using a black line; and b) The zero streamlines for $h/D = 0.33$ and $\dot{P}^* = 42$ (●), 43 (●), and 45 (●) for which $\dot{P}_o^* = 40$, and positions of the appearance of vortices in instantaneous field data based on the Γ_1 criteria for each case.*

assertion that the countercurrent shear layer leads to the initialization of ground vortices that are subsequently advected with the flow over the ground plane.

As noted above, the evolution of anchored ground vortices that are ingested into the inlet depends on sustained upstream flow in the countercurrent shear layer (otherwise the formed vortices are only advected downstream of the nacelle). To illustrate the subsequent evolution of the formed vortices in Figure 6b, the upstream and downstream advections of characteristic vortices are tracked in Figure 7a following their initial formation at $\dot{P}^* = 42$. The trajectory of the vortex that is advected downstream (denoted by open symbols) is aligned with the crosswind albeit with some spanwise meandering. The second trajectory (denoted by closed symbols) is of a vortex that eventually becomes anchored to and ingested into the inlet. Similar to the downstream-advected vortex, this vortex moves briefly downstream, then gradually changes its direction and begins to move away from the inlet face ($y = 0$), and at $x/R \approx 1.75$ it begins to move predominantly in the streamwise (x) direction towards the inlet. In connection with Figure 6a, it should be noted that the instantaneous upstream motion of this vortex (over a period of nominally 150 ms) must occur when the countercurrent shear layer migrates in the spanwise direction away from the inlet plane of the nacelle so that the wall-normal vortex is affected by the dominant upstream flow induced by the nacelle's suction. The present investigations show that at these formation parameters that are close to the formation boundary, the ingested vortices are highly unstable due to changes in the prevailing local flow direction and are temporarily ingested on the leeward side ($\theta \approx 135°$). As the suction into the inlet intensifies (higher $\dot{P}^*$), the ground vortex becomes more stable. Similarly, it was observed that when the height of the nacelle relative to the ground plane increases while a stable ground vortex is present at the inlet, weakening of the inlet suction effect near the surface leads to reduction in vortex circulation and migration of the ingested vortex towards the leeward inner lip of the nacelle followed by its eventual dislodging and streamwise advection.

The differences between the two types of vortices in Figure 7a are quantified by computing the variation of the circulation $\Gamma(r')$ of each vortex along its trajectory. The circulation about the vortex core is determined from the POD-reconstructed instantaneous successive velocity fields within a radius $r' = 0.15R$ about the vortex center using a line integral of the tangential velocity. The variation of $\Gamma(r')$ along each trajectory is shown in Figure 7b in terms of the number of time intervals between successive data frames (5 msec). These data show that, while the circulation of the vortex that is advected upstream towards the nacelle's inlet intensifies along its trajectory, the circulation of the vortex that is advected downstream remains significantly lower. It is interesting

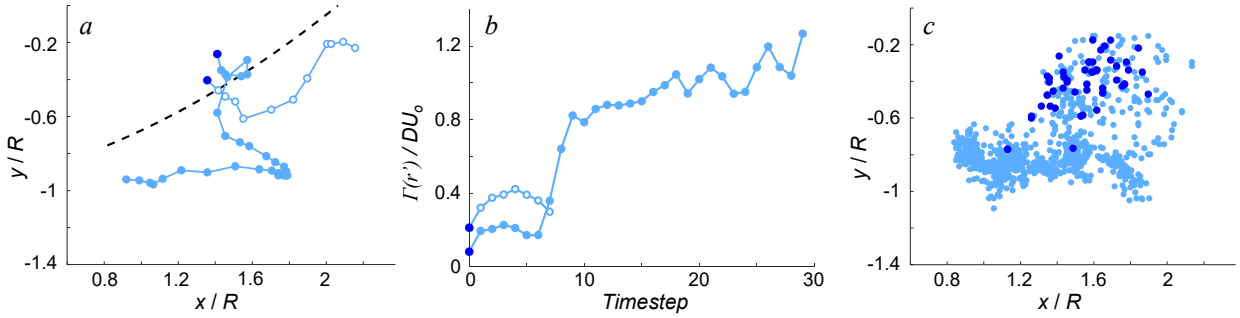

Figure 7. *Ground vortex trajectories using the Γ_1 criterion for h/D = 0.33 and $\dot{P}^* = 42$: a), Trajectories of vortices that are advected downstream (○) and upstream (●); b) The time history of the circulation of the vortices in (a) within a radius r' = 0.15R where each timestep is 5 ms; and c) The locations of the appearance (formation) of several vortices (●) and their subsequent positions (●).*

to note that the vortex that becomes anchored and ingested into the inlet intensifies as it moves *away* from the inlet before it is drawn laterally towards the inlet. These data indicate that concentrations of wall-normal vorticity by the countercurrent flow within the boundary layer are initially weak, but that the accumulation of wall boundary layer vorticity intensifies by suction as the pressure within the wall-normal vortices decreases. Furthermore, the vorticity concentrations that are advected into the wall-normal structures initially have both CW and CCW sense where the dominant wall-normal rotation is CCW and so the CW vorticity concentrations ultimately diffuse and cancel. As the wall-normal vortical structures intensify, the vorticity concentration within their cores is stretched along the centerline aided by the presence of axial flow as the core is drawn towards the inlet. The dispersion of upstream and downstream migrating wall-normal vortices for $\dot{P}^* = 42$ is demonstrated in Figure 7c that shows the first detection of a vortex (marked in blue) and detections of these vortices in subsequent frames are marked in light blue. As was discussed in connection with Figure 6b, the initial formation takes place in the vicinity of the *time-averaged* zero streamline and the map in Figure 7c shows clusters of vortices that are advected upstream within the domain $y/R < -0.6$ (when the instantaneous counter current layer migrates away from the nacelle's inlet plane) and vortices that are advected downstream within the domain $y/R > -0.6$. This points to similarity in trajectories of the ingested vortices where each of them must reach the outer, high velocity shear region near the surface to gain enough circulation that enables its upstream migration by the inlet suction.

IV. Flow Field of a Ground Vortex

The changes in the flow field at the nacelle's inlet plane with $\dot{P}^*$ below, at, and above the formation boundary of ground-normal vortices ($h/D = 0.33$, $\dot{P}^* = 23$, 42, and 82, cf. Figure 5a) are shown in Figure 8 using color raster plots of the time-averaged streamwise velocity $\bar{u}$ superposed with in-plane velocity vectors measured using planar PIV. At $\dot{P}^* = 23$, the interactions between the cross flow and suction flows are depicted by a local increase in $\bar{u}$ over the windward lip of the inlet (on the left) followed by a monotonic reduction from left to right towards the leeward edge as the cross flow is turned into the nacelle. At $\dot{P}^* = 42$ (Figure 8b), the flow over the windward lip of the inlet intensifies, with a domain of reversed $\bar{u}$ near the ground plane on the leeward side, as discussed by Nichols et al. (2023). The boundary between the forward and backward $\bar{u}$ is marked by a dashed line where this reversed flow contributes to the upstream flow in the shear layer (c.f. Figure 6a). At $\dot{P}^* = 82$ an anchored ground vortex is present and the reversal in the streamwise velocity is more apparent as is evidenced by the upstream migration of the streamwise boundary (dashed line). The presence of the CW vortex (cf. Figure 3a) on the lower segment of the nacelle's lip is marked by a local maximum of $\bar{u}$ at $(x/R,\ z/R) = (0.10,\ -0.63)$ and a local minimum at $(x/R,\ z/R) = (0.17,\ -0.87)$ indicating that the center of the core is located ~$0.25R$ above the nacelle's lip.

The boundary between the downstream and upstream intake flow is examined in greater detail in Figure 8d, that focuses on the vanishing streamwise velocity component underneath the inlet (i.e., up to $z/R = -1$). It is also noted that such a boundary does not exist for the case of the lowest momentum flux since no reversed flow is present underneath the nacelle (cf. Figure 8a). As the inlet momentum flux increases, this boundary migrates upstream while always exhibiting a characteristic deficit closest to the ground plane as the flow near the wall transitions to upstream orientation. At the highest momentum flux case of $\dot{P}^* = 197$, the flow wraps around the top of the nacelle and becomes ingested into the inlet as discussed by Nichols et al. (2023) which introduces

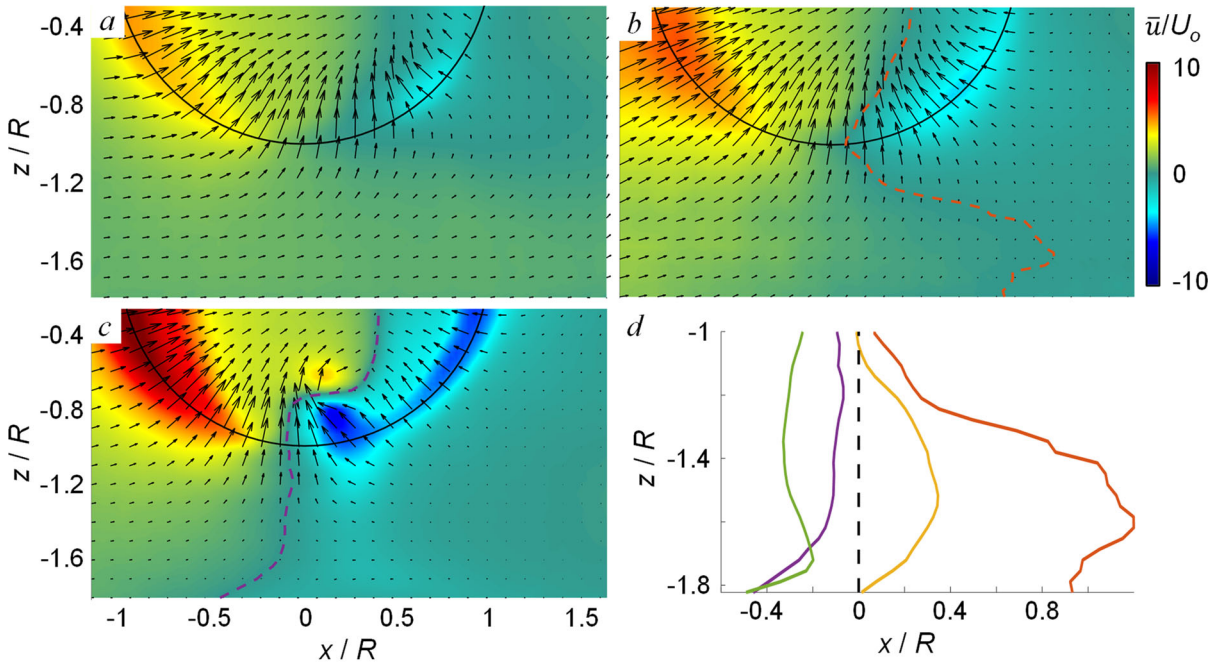

Figure 8. *Color raster plots of the time-averaged streamwise velocity $\overline{u}$ overlaid with in-plane velocity vectors at the inlet face for h/D = 0.33 and $\dot{P}^*$ = 23 (a), 42 (b), and 82 (c). The boundary of $\overline{u}$=0 is shown for reference in (b) and (c) and plotted in (d) for $\dot{P}^*$ = 42 (●), 61 (●), 82 (●), and 197 (●).*

significant upstream momentum near the wall and pushes this boundary past the inlet centerline while also changing the concavity of the bulk of the profile.

From the previous analysis, it is apparent that, as the inlet momentum flux increases, the anchored vortex at the inlet plane moves farther upstream towards the windward side of the inlet. Nichols et al. (2023) showed that as the vortex migrates upstream, it diminishes in strength and ultimately reverses its sense before it is expelled from the inlet. The present PIV measurements at the inlet plane are used to determine the distributions of the locations of the instantaneous ground vortices within the inlet using the Γ_1 criteria for $\dot{P}^* = 61$, 82, and 197 ($h/D = 0.33$). The corresponding clusters of the centerlines (Figure 9a) show that for each momentum flux, the vortex cores exhibit mainly scatter in azimuthal position: $\dot{P}^* = 61$: $138° < \theta < 151°$, $\theta_{mean} = 144°$; $\dot{P}^* = 82$: $155° < \theta < 171°$, $\theta_{mean} = 165.4°$; and $\dot{P}^* = 197$: $165° < \theta < 186°$, $\theta_{mean} = 172°$. The corresponding histograms of the azimuthal and radial positions are shown in Figures 9b and c, respectively. The histograms of the azimuthal positions (Figure 9b) exhibit an approximately normal distribution for $\dot{P}^* = 61$ while the other two distributions are skewed towards the windward and leeward sides for $\dot{P}^* = 82$ and 197, respectively. The radial distributions for $\dot{P}^* = 61$ and 197 are relatively narrow, while for $\dot{P}^* = 82$ there is a clear skew towards the inlet centerline. These differences are explained by the earlier observation of Nichols et al. (2023) who reported that, as the inlet momentum flux increases, the vortex formation is preceded by closing of the nacelle's near wake to the ground. Further increase of the momentum flux ultimately leads to the ingestion of the wake as the flow wraps around the top of the inlet and eventually moves into the inlet. For $\dot{P}^* = 82$, the wake is closed but not ingested while at $\dot{P}^* = 197$ the wake becomes ingested. It is argued that the process of wake ingestion acts as the barrier preventing azimuthal motion around $\theta = 172°$.

The structure of the flow in the vicinity of the nacelle in the presence of an anchored vortex is investigated using stereo PIV in multiple cross stream planes that are normal to the ground plane and parallel to the inlet plane of the nacelle (cf. Figure 2c). The spanwise (y) spacings of these planes (along the axis of the nacelle) is equal to x-z grid spacing within each plane. These data are used to construct the 3-D time-averaged flow fields within the domain: $-1.15 \le x/R \le 1.64$, $0.06 \le y/R \le 1.56$, and $-1.82 \le z/R \le -0.26$. To illustrate the flow associated with the ground vortex, the 3-D flow field is illustrated using the trajectories of particles that are "seeded" near the ground plane to produce the pathlines shown in Figure 10. For $\dot{P}^* = 23$, in the absence of an anchored vortex (Figure 10a, cf. Figure 5a), the particles that originate near the ground plane are slightly lifted off the surface as they are advected downstream but are not carried into the inlet. As the inlet momentum flux is raised to just above the critical value to $\dot{P}^* = 42$ (Figure 10b), the intermittent formation of wall-normal vortices near the ground plane that are advected upstream is manifested by notable liftoff and turning of seeded flow upstream of the inlet that is ingested along the inlet's lower leeward side which interacts with flow from underneath the inlet that is advected straight up and ingested along the lower half of the inlet face. This flow field is associated with the countercurrent flow over the ground plane that spawns the initial formation of the vortical structures (c.f. Figure 6). Finally, if the inlet momentum flux is sufficiently high ($\dot{P}^* = 82$, Figure 10c), an anchored ground vortex is formed whose core is entirely seeded from flow along the ground plane where the inner core is seeded by particles that originate from directly underneath the inlet. Since particle positions are spaced at fixed time increments, increased spacing along the trajectories near the inlet face indicates increased local speed. The concurrent narrowing of the trajectories bundle indicates vortex stretching as it is ingested into the inlet.

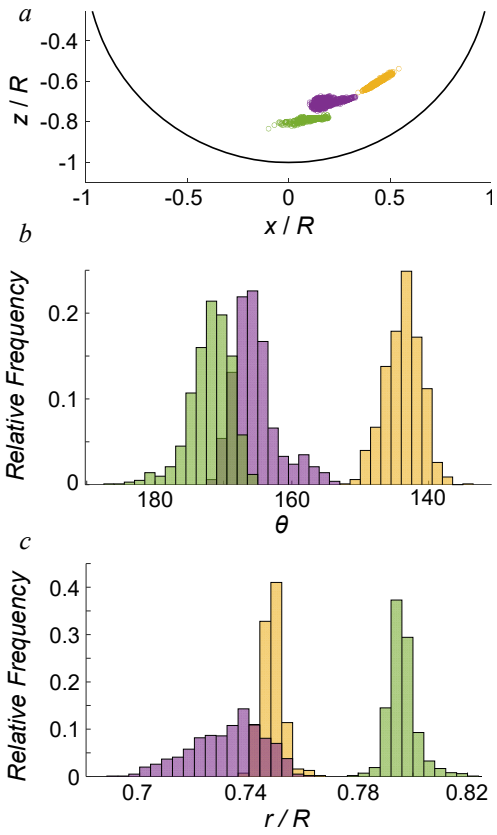

Figure 9. *a) Locations of the ground vortex within the inlet as determined by the Γ_1 criteria for h/D = 0.33 and $\dot{P}^*$ = 61 (●), 82 (●), and 197 (●); and Histograms of the azimuthal (b) and radial (c) positions.*

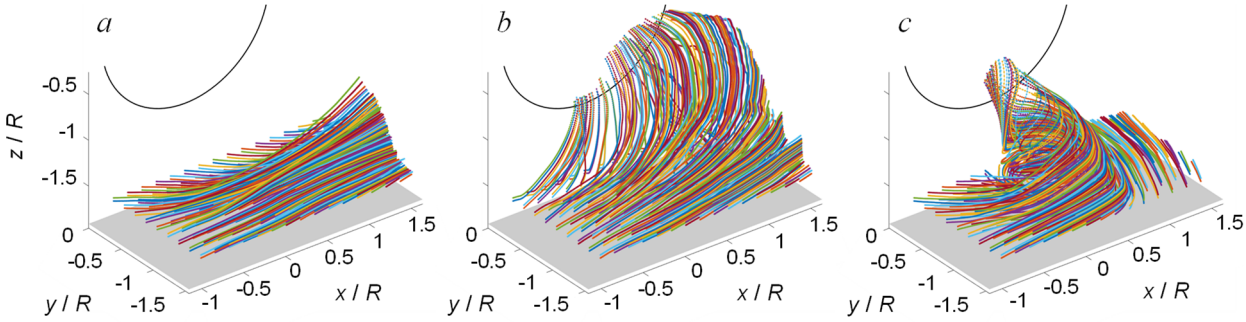

Figure 10. *Pathlines of particles seeded near the ground plane for h/D = 0.33 and $\dot{P}^*$ = 23 (a), 42 (b), and 82 (c). The dimensionless time increment along the trajectories is $\Delta t\, U_o/D = 0.0026$.*

The flow field in the presence of the anchored vortex provides some insight into the transport of vorticity from the wall boundary layer above the ground plane along the anchored vortex. The spanwise and wall-normal components of vorticity are considered. Since the only source of vorticity is from the wall layer, it is informative to extract the dominant spanwise vorticity domains that sustain the ground vortex (Figure 11a). Isosurfaces of spanwise vorticity $|\omega_y D/U_o| = 20$ of opposite sense near the ground plane demonstrate the turning and tilting of the entrained predominantly CW spanwise vorticity from the wall layer. In the fixed coordinate system, as this vorticity is scooped from the wall layer, it leads to the formation of counterrotating, opposite sense spanwise vorticity concentrations that are continuously ingested into the wall-normal vortex core and are advected along its core aiding in its sustainment. Resulting from this entrainment, the vorticity is reoriented such that the spanwise vorticity transitions into the wall normal component (Figure 11b). The isosurface of $\omega_z D/U_o = 75$ results from the entrainment, tilting, and stretching of the wall layer vorticity concentrations. Owing to the bending of the vortex centerline, the wall normal component diminishes as the vortex approaches the nacelle and transitions into spanwise vorticity in the laboratory's frame of reference denoted by the appearance of a vorticity isosurface of equal magnitude in Figure 11a at about $z/R = -1.2$ which keeps expanding further into the inlet.

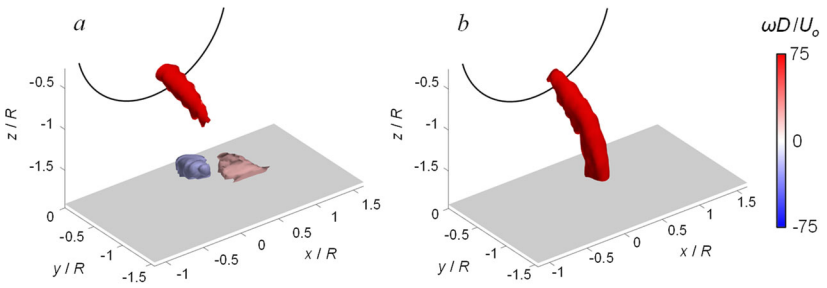

Figure 11. *a) Spanwise, ω_y, and b) Wall normal, ω_z, vorticity isosurfaces for $\omega D/U_o$ = -20 (●), 20 (●), and 75 (●) at h/D = 0.33 and $\dot{P}^* = 82$.*

The complexity of the vorticity concentrations in the flow that surrounds the anchored vortex is depicted using color raster plots of spanwise vorticity overlaid with in-plane velocity vectors in a vertical section through the vortex core at three levels of momentum flux $\dot{P}^* = 61$, 82, and 197 ($h/D = 0.33$, Figures 12a-c, respectively). Since the vortex core moves towards the inlet plane as $\dot{P}^*$ increases, the respective positions of the PIV planes are set at $y/R = -0.75$, -0.6, and -0.44. The velocity field clearly shows the uplift of the cross flow towards the nacelle and the CW spanwise vorticity layer upstream of the anchored vortex. The magnitude of this vorticity component is nearly independent of the intake speed averaging around $\omega_y D/U_o = 6$ for the three cases indicating that the upstream spanwise vorticity is solely a function of the crosswind speed. Figure 12a shows two opposite sense concentrations of spanwise vorticity near the core of the CW wall-normal

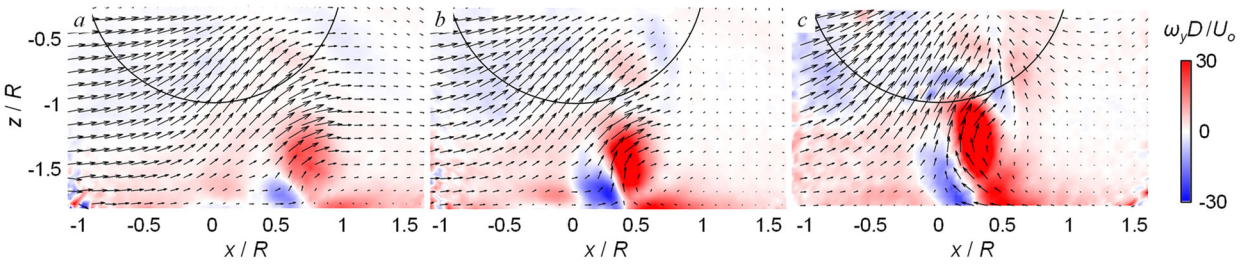

Figure 12. *Color raster plots of time-averaged spanwise vorticity concentrations (axial relative to the inlet) ω_y, overlaid with velocity vectors of the in-plane velocity components, for h/D = 0.33 and $\dot{P}^* = 61$ (a), 82 (b), and 197 (c) measured at planes through the center of the vortex core at y/R = -0.75 (a), -0.60 (b), and -0.44 (c).*

vortex. The downstream concentration is apparently formed by transport of CW spanwise vorticity towards the nacelle while the smaller CCW spanwise vorticity is the result of turning around the vortex core which is pushed towards the surface by the oncoming flow owing to blockage by the wall-normal vortex. *The center of the core of the wall-normal ground vortex is marked by the gap between the two-opposing vorticity concentrations.* As the momentum flux increases, the two opposite spanwise vorticity concentrations near the wall are intensified while the flow downstream of the vortex appears to be increasingly directed into the plane (towards the nacelle) apparently the result of the obstacle presented by the vortex itself. It is also interesting to note that for the highest momentum flux case ($\dot{P}^* = 197$), there is an intensification of CCW spanwise vorticity above the vortex which also bounds its upper-downstream side. This vorticity concentration is what prevents the vortex from moving towards the leeward side resulting in the windward skew of the vortex at this condition (c.f. Figure 9b). These data also show that as the momentum flux increases (Figures 12a-c), the ground vortex displaces both towards the inlet face (y/R = -0.75, -0.6, and -0.44) and upstream towards the centerline (x/R = 0.71, 0.37, and 0.27). In addition, both vorticity concentrations grow outward which is attributed to the increased ground vortex circulation which induces a lower pressure at its core and scoops additional wall layer flow into the vortex.

V. Ground Vortex Characterization

Since the dominant vorticity component of a ground vortex is aligned with the vortex axis, the vortex evolution is also assessed in terms of the vorticity variation along its centerline. The vortex center is identified using the Γ_1 criterion in each plane of the stereo PIV dataset (c.f. Figure 10) using the procedure discussed in connection with Figure 6b. The center of the vortex in each plane is identified by using an area-weighted average of Γ_1 above a predetermined threshold from the 3-D data grid; this process is also repeated in horizontal planes (parallel to the ground plane) as shown in Figure 13a. The centerline of the vortex core is computed between the ground and inlet using a second order polynomial fit through these points. Polynomial fits through the points $x(y)$ and $z(y)$ yield the streamwise and spanwise variations with height. When used together, the planar position of the vortex as a function of the distance from the ground plane is expressed using the two equations to produce a 3-D polynomial fit through the core (Figure 13a). The three vortex centerlines for $\dot{P}^* = 61$, 82, and 197 (h/D = 0.33) are plotted in perspective views in Figure 13b and show how the ground vortex moves towards the windward side of the nacelle and towards the bottom inlet lip within the inlet as it moves closer to the inlet face with the increase in $\dot{P}^*$.

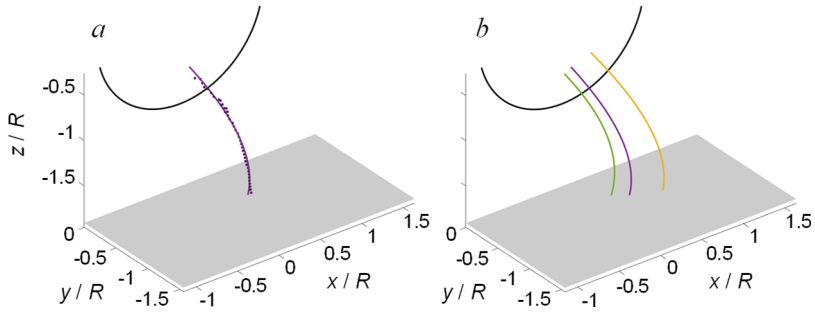

Figure 13. *Time-averaged vortex centerline location as determined by the Γ_1 criteria at multiple planes to create a 3D reconstruction of the vortex centerline for h/D = 0.33 and $\dot{P}^*$ = 82 (●) (a), and the centerlines for $\dot{P}^*$ = 61 (●), 82 (●), and 197 (●) (b).*

Once the vortex centerlines are extracted, a tangent to the centerline at equally distributed points is determined to define the local vorticity component within the projected flow field in the plane defined by the tangent. To achieve this, a data grid is formed in the plane having identical spacings

to the grid spacing of the collected data ($dx \times dz$) and the three velocity components measured relative to the tunnel coordinate system are interpolated onto the new grid and projected onto the local, vortex aligned coordinate system. Aside from the in-plane velocity components, the plane-normal (third) velocity component aligned with the local vortex axis is also computed. The evolution of distributions of the axial vorticity in multiple planes along the centerline of the vortex at $\dot{P}^* = 82$ is shown in Figure 14 using color raster plots. These data show that the core axial vorticity increases as the vortex cross section approaches the inlet, reaching levels of about $\zeta D/U_o \approx 250$. This intensification of the vorticity within the core is in accord with the prior observation of the convergence of particle paths as they are ingested into the inlet (Figure 10c), as the vortex is stretched.

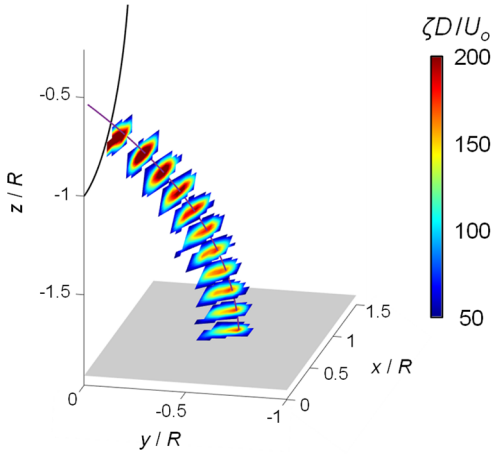

Figure 14. *Time-averaged vortex vorticity along the vortex centerline, ζ, on equally spaced planes for h/D = 0.33 and $\dot{P}^* = 82$.*

In addition to the axial vorticity, the evolution of other characteristic parameters of the vortex are also considered. The variation of the axial velocity along the vortex centerline, in terms of the vertical coordinate z ($z = 0$ at the inlet axis) is shown in Figure 15a for $\dot{P}^* = 61$, 82, and 197. Near the ground, the axial velocity component of these vortices is approximately equal to the crosswind speed as the cross flow is initially lifted off the ground and into the vortex. As the vortex extends above the surface, there are three distinct regions of the evolution of its axial velocity. Close to the ground, the vortex-core velocity increases at a rate that is proportional to the inlet momentum flux. This rate increases from $(V_n/U_o)/(z/R) = 1.96$ for the lowest momentum flux ($\dot{P}^* = 42$) up to $(V_n/U_o)/(z/R) = 5.67$ for the highest ($\dot{P}^* = 197$); however, each of these rates is significantly lowered past $z/R \approx -1.6$, before resuming a steeper rate past $z/R \approx -1.4$. This increase in the velocity gradient closer to the inlet is attributed to the suction effect of the intake flow, which not only increases with the increase in the inlet momentum flux, but also with the proximity of the vortex core to the inlet face with the increase in $\dot{P}$. Of particular interest is assessing the variation in the vortex circulation along its centerline that is computed as described in Figure 7b; however, unlike in Figure 7b, the total circulation is calculated rather than the circulation representing the vortex core. Therefore, for each plane normal to the vortex centerline, the circulation is assessed within circles of increasing radii around the vortex center until each reaches saturation. The resulting evolution of circulation is shown in Figure 15b, which indicates a nearly-invariant circulation along the core of each vortex. Clearly, the circulation magnitude increases with $\dot{P}^*$, but for each established vortex off the ground plane, there is no significant change along its centerline suggesting that the main source of the ground vortex vorticity is indeed off the ground plane, as discussed in connection with Figure 11.

The saturation of the circulation level at each vortex plane that is used to define the corresponding vortex radius is used to define the evolution of the characteristic scale of the vortex along its core. The vortex characteristic radius is estimated as the radial distance away from the center at which the circulation value level first reaches $0.95\Gamma_{max}$. Based on Figure 10c, it is known that the vortex scale decreases while it is being ingested into the inlet, which is quantified in Figure 15c. Again,

a clear trend in the reduction in the vortex scale is seen with the increase in the inlet momentum flux, while each vortex undergoes a similar stretching along its centerline. The initial and terminal states are characterized by a reduced rate of decrease, while the highest slope in dR_v/dz is measured along most of the centerline. Furthermore, the decrease in vortex radius over the measured centerline is about 34%, 29% and 20% for $\dot{P}^* = 61$, 82, and 197, respectively. Finally, the volume flow rate through each vortex is calculated based on the radius as an indicator of the vortex entrainment. The volume flow rate at each plane is estimated from the out-of-plane (vortex-axial) velocity component at each grid point within the vortex radius. The resulting evolution of the vortex axial flow rate (Figure 15d) indicates a rather substantial and nearly steady increase between the ground surface and the inlet ($z/R = -1$) in the excess of 80% for each of the three momentum fluxes. The volume flow rates through the vortices are about 3.3%, 3.6%, and 3.2% of the inlet flow rate for $\dot{P}^* = 61$, 82, and 197, respectively. Thus, for a given crosswind speed, the axial flow rate carried into the inlet by the ground vortex appears to be dependent only on the inlet volume flow rate.

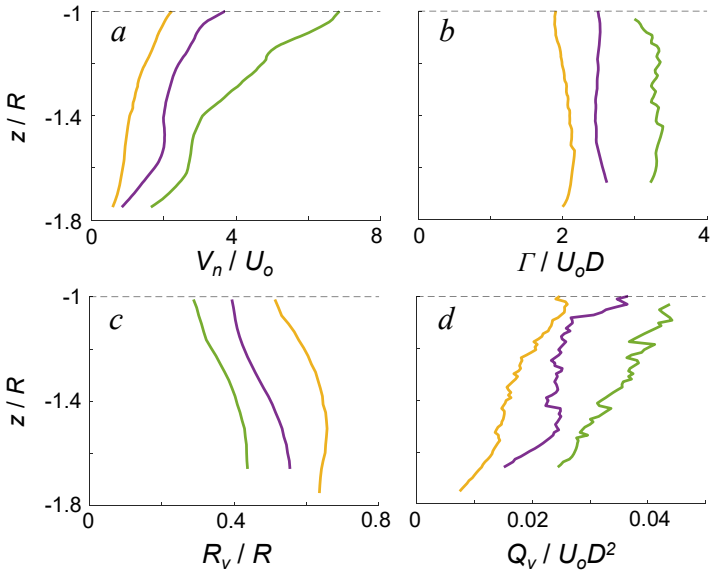

Figure 15. *Measurements of the centerline normal velocity (a), circulation (b), radius of the vortex (c), and vortex flow rate (d) along the vortex centerline for h/D = 0.33 and $\dot{P}^*$ = 61 (●), 82 (●), and 197 (●).*

VI. Conclusions

The current wind tunnel investigations focus on the formation and sustainment of a ground vortex in a cross flow normal to an axisymmetric nacelle near a ground plane. These investigations build on the earlier works of Nichols et al. (2022, 2023) who showed that these vortices originate within a counter-current shear flow that forms over the ground plane on the leeward side of the nacelle and demonstrated the viability of a formation map that predicts the formation of wall-normal vortices based on the dimensionless momentum flux into the nacelle and the nacelle's distance from the ground plane. The present investigations show that two types of wall-normal vortices are initiated at the critical parameter range (or boundary) for vortex formation, as a result of the countercurrent interactions between the cross flow and the nacelle suction flow. The wall-normal vortical motions gain circulation only while being advected over the high vorticity domains of the boundary layer flow over the ground plane. It is argued that following the intensification of the wall-normal vortical structures, the vorticity concentration within their cores begin to stretch toward the nacelle's inlet and are aided by the presence of axial flow along the vortex centerline as its core is drawn towards the inlet to fully form an anchored, ingested ground vortex. If the wall-normal vortical structures do not intensify along their trajectory, they are advected downstream and do not reach the inlet. As the dimensionless momentum flux of the inlet flow increases, the ground vortex remains 'anchored' to the inlet and is sustained by transport of vorticity from the

surface vorticity layer, although the azimuthal location of its ingestion shifts upstream and towards the bottom inlet lip of the nacelle's inlet with minimal changes in the radial position of the vortex core.

A three-dimensional reconstruction of the flow field of a ground vortex shows that the vortex is sustained by entrainment of spanwise vorticity concentrations from the surface layer that are tilted and stretched into the vortex and become aligned with its core. It is shown that, for a given inlet momentum flux, the circulation of the anchored ground vortex about its centerline is invariant along the core as the vortex is stretched into the inlet, but the magnitude of the circulation increases with the momentum flux into the nacelle. Furthermore, the decrease in the vortex diameter that is associated with the stretching along the core is inversely proportional to the inlet's dimensionless momentum flux, while the fraction of the volume flow rate that is advected through the vortex core into the inlet at a given crosswind speed appears to be dependent only on the flow rate into the inlet.

Acknowledgment

This research has been supported by Georgia Tech. The support of the Boeing Company in the development of the crosswind facility is gratefully acknowledged.

References

Berkooz, G., Holmes, P. and Lumley, J. L., "The proper orthogonal decomposition in the analysis of turbulent flows," *Annual Review of Fluid Mechanics*, Vol. 25, pp. 539-575, 1993. https://doi.org/10.1146/annurev.fl.25.010193.002543

Brix, S., Neuwerth, G., and Jacob, D., "The Inlet-Vortex System of Jet Engines Operating near the Ground," AIAA Paper 2000-3998, August 2000. https://doi.org/10.2514/6.2000-3998

Colehour, J. L., and Farquhar, B. W., "Inlet Vortex," *Journal of Aircraft*, Vol. 8, No. 1, 1971, pp. 39–43. https://doi.org/10.2514/3.44224

Graftieaux, L., Michard, M. and Grosjean, N., "Combining PIV, POD and vortex identification algorithms for the study of unsteady turbulent swirling flows," *Measurement Science and Technology*, Vol. 12, No. 9, pp. 1422-1429, 2001. https://doi.org/10.1088/0957-0233/12/9/307

Huang, Y. and Green, M. A., "Detection and tracking of vortex phenomena using Lagrangian coherent structures," *Experiments in Fluids*, Vol. 56, No. 7, pp. 1-12, 2015. https://doi.org/10.1007/s00348-015-2001-z

Johns, C., "The Aircraft Engine Inlet Vortex Problem," AIAA Paper 2002-5894, October 2002. https://doi.org/10.2514/6.2002-5894

Klein, H., "Small Scale Tests on a Jet Engine Pebble Aspiration," Douglas Aircraft Co., Inc., Santa Monica Division, Publication SM 14895, 1953

Liu, W., Greitzer, E. M., and Tan, C. S., "Surface Static Pressures in an Inlet Vortex Flow Field," *Journal of Engineering for Gas Turbines and Power*, Vol. 107, No. 2, 1985, pp. 387–393. https://doi.org/10.1115/1.3239738

Murphy, J. P., MacManus, D. G., and Sheaf, C. T., "Experimental Investigation of Intake Ground Vortices during Takeoff," *AIAA Journal*, Vol. 48, No. 3, 2010, pp. 688–701. https://doi.org/10.2514/1.45896

Murphy, J. P., and MacManus, D. G., "Ground Vortex Aerodynamics under Crosswind Conditions," *Experiments in Fluids*, Vol. 50, No. 1, 2011, pp. 109–124. https://doi.org/10.1007/s00348-010-0902-4

Nakayama, A., and Jones, J. R., "Vortex Formulation in Inlet Flow near a Wall," AIAA Paper 96-0803, January 1996. https://doi.org/10.2514/6.1996-803

Nakayama, A., and Jones, J. R., "Correlation for Formation of Inlet Vortex," *AIAA Journal*, Vol. 37, No. 4, 1999, pp. 508–510. https://doi.org/10.2514/2.743

Nichols, D. A., Vukasinovic, B., Glezer, A., DeFore, M. C., Rafferty, B., and Palacios, F. D., "Characterization and Control of Nacelle Inlet Flow in Crosswind," AIAA Paper 2019-3685, June 2019. https://doi.org/10.2514/6.2019-3685

Nichols, D. A., Vukasinovic, B., Glezer, A., and Rafferty, B, "Formation of a Nacelle Inlet Ground Vortex in Crosswind," AIAA Paper 2022-1698, January 2022. https://doi.org/10.2514/6.2022-1698

Nichols, D. A., Vukasinovic, B., and Glezer, A., "Scaling Characteristics of Ground Vortices in a Nacelle Inlet Flow Field," AIAA Paper 2023-1981, January 2023. https://doi.org/10.2514/6.2023-1981

Rodert, L. A., and Garrett, F. B., "Ingestion of Foreign Objects into Turbine Engines by Vortices," NACA TN 3330, February 1955.

Shin, H. W., Greitzer, E. M., Cheng, W. K., Tan, C. S., and Shippee, C. L., "Circulation Measurements and Vortical Structure in an Inlet-Vortex Flow Field," *Journal of Fluid Mechanics*, Vol. 162, No. 8, 1986, pp. 463–487. https://doi.org/10.1017/S0022112086002124

Shmilovich, A., and Yadlin, Y., "Engine Ground Vortex Control," AIAA Paper 2006-3006, June 2006. https://doi.org/10.2514/6.2006-3006

Shmilovich, A., and Yadlin, Y., "Flow Control Techniques for Transport Aircraft," *AIAA Journal*, Vol. 49, No. 3, 2011, pp. 489–502. https://doi.org/10.2514/1.J050400

Siervi, F. D., "A Flow Visualization Study of the Inlet Vortex Phenomenon," Massachusetts Institute of Technology, Gas Turbine and Plasma Dynamics Laboratory, GT & PDL Report No. 159. 1981.

Siervi, F. D., Viguier, H. C., Greitzer, E. M., and Tan, C. S., "Mechanisms of Inlet-Vortex Formation," *Journal of Fluid Mechanics*, Vol. 124, 1982, pp. 173–207. https://doi.org/10.1017/S0022112082002456

Sirovich, L., "Turbulence and the dynamics of coherent structures. Part I: Coherent structures," *Quarterly of Applied Mathematics*, Vol. 45, No. 3, 1987, pp. 561-571.

Trapp, L. G., Argentieri, H. G., de Souza, F. J., and Girardi, R. da M., "Aspects of Isolated Nacelles Near the Ground During Crosswind Operation," ENCIT Paper CIT06-0740, December 2006.

Trapp, L. G., and Girardi, R., "Evaluation of Engine Inlet Vortices Using CFD," AIAA Paper 2012-1200, January 2012. https://doi.org/10.2514/6.2012-1200